



## Dynamics and deposits generated by the Kos Plateau Tuff eruption: Controls of basal particle loss on pyroclastic flow transport

**Josef Dufek**

*Department of Earth and Planetary Science, University of California, Berkeley, 307 McCone Hall, Berkeley, California, 94720, USA (dufek@berkeley.edu)*

**George W. Bergantz**

*Department of Earth and Space Science, University of Washington, Box 351310, Seattle, Washington, 98195, USA (bergantz@u.washington.edu)*

[1] The explosive eruption of voluminous silicic magmas often produces widespread and massive deposits formed from pyroclastic density currents. While these punctuated events dramatically alter the landscape and have potential climate-altering impact, our understanding of the internal structure and transport dynamics of these eruptions is hampered by a lack of direct observations. We utilize the natural boundary conditions encountered by the eruption of the Kos Plateau Tuff to probe its internal structure as well as constrain the neotectonic activity in the region and eruption duration of this moderate to large ( $>60 \text{ km}^3$ ) event. At the time of the eruption, 161 ka, the lower sea level in the Mediterranean may have resulted in flows that traversed mostly land to the north of the eruptive vent, while flows to the south may have encountered an expanse of water. Steep topography and overwater transport can impede the transport of the dense basal portions of the flow where particles make multiple or sustained contact with the bed. We use an Eulerian-Eulerian-Lagrangian computational approach coupled with overwater and overland boundary conditions, including topography, to determine the role of bed load versus suspended load in the transport of these flows. We find that a ring vent structure and eruptive fluxes greater than  $\sim 2 \times 10^6 \text{ m}^3/\text{s}$  are required for the spatial distribution of the KPT. The maximum grain size and deposit locations of the first voluminous ignimbrite unit (D) can be explained by suspended flow to the south, consistent with overwater transport, and bed load and suspended load transport to the north, consistent with overland transport. However, the maximum lithic size for the largest and last ignimbrite unit (E) requires some bed load transport in all directions. We propose that the boundary conditions were significantly altered during the course of the eruption, through either the in-filling of a shallow sea to the south or the development of a thick pumice raft to aid saltation. On the basis of the inferred eruptive flux, we estimate that the duration of the eruption climax, in which most of the material was erupted, likely only lasted from a few hours to a day.

**Components:** 9324 words, 13 figures, 2 tables.

**Keywords:** pyroclastic flow; eruption dynamics; Aegean volcanism; bed load; suspended load; caldera-forming eruption.

**Index Terms:** 8428 Volcanology: Explosive volcanism; 8404 Volcanology: Volcanoclastic deposits; 8440 Volcanology: Calderas.

**Received** 2 July 2007; **Revised** 18 September 2007; **Accepted** 12 October 2007; **Published** 21 December 2007.

Dufek, J., and G. W. Bergantz (2007), Dynamics and deposits generated by the Kos Plateau Tuff eruption: Controls of basal particle loss on pyroclastic flow transport, *Geochem. Geophys. Geosyst.*, 8, Q12007, doi:10.1029/2007GC001741.

## 1. Introduction

[2] The largest known eruption of the south Aegean Arc produced the Kos Plateau Tuff (161 ka) with over 60 km<sup>3</sup> of rhyolitic material, DRE [Allen, 2001]. Similar to other moderate to large volume eruptive deposits, the Kos Plateau Tuff is dominated by voluminous ignimbrites, inferred to be emplaced by pyroclastic flows formed during eruptive column collapse [Allen, 2001; Allen and Cas, 2001]. While voluminous ignimbrites are relatively abundant in the geologic record, many aspects of the transport and emplacement mechanisms responsible for their origin remain poorly constrained [Branney and Kokelaar, 2002; Wilson and Hildreth, 2003]. It is apparent that these ground-hugging flows are sensitive to topographic features [Fisher et al., 1993]; however, the way in which the spatiotemporal variability in flow concentration as well as the runout distance reacts to variable bed conditions is a source of uncertainty in conceptual and numerical models of pyroclastic flow transport [Branney and Kokelaar, 2002; Dobran et al., 1994; Fisher et al., 1993; Valentine and Wohletz, 1989]. The Kos Plateau Tuff eruption may have been the site of both overwater and overland transport of pyroclastic flows, providing the opportunity to distinguish different transport mechanisms from a single eruption [Allen and Cas, 2001].

[3] During eruption, pyroclastic flows are likely vertically graded in particle volume fraction (highest concentration near the bed) due to gravitational settling and entrainment of ambient atmosphere [Branney and Kokelaar, 1997; Valentine, 1987]. Enhanced particle-concentration near the bed (bed load) exceeding values from gravitational settling alone, can develop when transport conditions favor saltation (multiple particle-bed collisions) and frictional contact between particles and the bed, often in high shear-stress conditions [Cagnoli and Manga, 2004]. This results in much greater particle concentration and momentum flux near the bed compared to flows maintained only by turbulent suspension (suspended load) [Dufek and Bergantz, 2007]. As the particle volume fraction and momentum flux ultimately determine the destructive force of these flows, a better understanding of pyroclastic flow-bed coupling is necessary for

more accurate hazard assessments as well as interpreting deposits of previous eruptions.

[4] The transport of pyroclastic flows over bodies of water may provide a way to better understand the portion of a pyroclastic flow that comes in contact with the bed versus that which is primarily suspended before deposition. The abundance of volcanoes near bodies of water has resulted in numerous historic and preserved eruptions that have traversed large bodies of water [Allen and Cas, 2001; Burgisser, 2004; Carey et al., 1996; Druitt and Francaviglia, 1992; Fisher et al., 1993; LaCroix, 1904; Miller and Smith, 1977; Robin et al., 1994]. Many other overwater eruptions have likely occurred, but remain obscured due to lack of substantial subaerial deposit exposure. A number of interactions may occur at a pyroclastic flow-water interface as revealed by analog experiments [Freundt, 2003] and numerical simulations [Dufek and Bergantz, 2007; Dufek et al., 2007], including phase change at the water surface and loss of mass and momentum of pyroclastic particles that settle through the water surface. Tsunami, primarily generated from water displacement as pyroclastic flows enter the ocean, are one example of a momentum transfer mechanism with far-reaching consequences [Carey et al., 1996; Mattioli et al., 2007; Watts and Waythomas, 2003]. Steam explosions, or littoral blasts, can be generated when pyroclastic flows first enter the water provided the grain size distribution is fine enough that energy transfer from particle to water is rapid [Dufek et al., 2007; Edmonds and Herd, 2005; Mastin and Witter, 2000; Zimanowski et al., 1997]. In the far field, the loss of particles through the water surface, i.e., a leaky boundary, can also significantly impact the concentration and runout distance of a pyroclastic flow [Dufek and Bergantz, 2007].

[5] We perform a series of numerical simulations of the Kos Plateau Tuff eruption to better understand the role of bed load and suspended load in large ignimbrite forming eruptions as well as to provide an additional constraint to the ongoing discussion of the neotectonic and sea level history of the eastern Aegean. We consider the effect of both leaky (overwater) and saltation (overland) boundaries on the dynamics and deposit distribu-

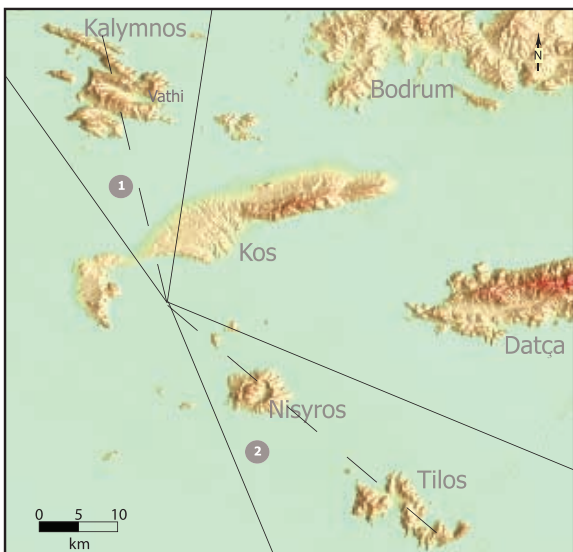


**Figure 1.** Map of Kos, Greece. The solid lines denote the region considered by the three-dimensional simulations, and the dashed lines indicate the track of the two-dimensional simulations. The area to the north of Kos (1) was modeled entirely with saltation boundary conditions, while the area to the south (2) was modeled using leaky boundary conditions in the regions where water is currently present. The island of Nisyros was not present at the time of the KPT eruption, and this area is also considered using leaky boundary conditions.

tions of these flows. The present deposits of the Kos Plateau Tuff, especially distal deposits, are primarily valley-ponded and influenced substantially by regional topography. To provide comparison between the observed deposits and the numerical simulations we performed a suite of two-dimensional and three-dimensional simulations to assess the role of both topography and overwater/overland conditions on the transport of these flows. In section 2 we review the stratigraphic framework of the Kos Plateau Tuff deposits, focusing on the voluminous unit D and E ignimbrites. We then develop an Eulerian-Eulerian-Lagrangian numerical model in section 3. We apply this approach in two-dimensions over a broad range of parameters in section 4 to constrain the effect of vent parameters and compare the simulations with known depositional patterns. In section 5 we extend this approach to three-dimensions for a more detailed assessment of deposit distribution, flow dynamics and the dispersal of lithic clasts. These results constrain the eruptive flux, duration of the eruption and the nature of the boundary conditions

over which flows were transported as discussed in sections 6 and 7.

## 2. Geologic Setting and Stratigraphic Overview

[6] Sea level reconstructions suggest that the Kos Plateau Tuff eruption may have produced pyroclastic flows that traversed both land and water during a single eruptive episode [Allen and Cas, 2001]. The Mediterranean sea level 161 ka was likely 60–80 m lower than current conditions and the shallow sea to the north of the island of Kos and extending to Kalymnos (Figure 1) was likely subaerially exposed [Allen and Cas, 2001]. On the basis of this reconstruction, Allen and Cas [2001] also inferred that flows to the south and deposited on the island of Tilos and the Turkish peninsula of Datca traveled primarily over open water.

[7] To help clarify the neotectonic and sea level history a seismic reflection experiment was conducted by Pe-Piper *et al.* [2005]. Seismic reflection profiles in the West Kos Basin (between Kos and Nisyros) indicate offset of acoustically incoherent deposits interpreted to be the Kos Plateau Tuff that Pe-Piper *et al.* [2005] have hypothesized is a result of neotectonic subsidence along a series of east-west faults. However, it is difficult to discern how much subsidence in this area is a result of caldera collapse or post-eruptive neotectonic subsidence. On the basis of this offset, Pe-Piper *et al.* [2005] suggest much of the area between Kos and Tilos was either a shallow marine environment or subaerially exposed, in contrast with the Allen and Cas [2001] interpretation.

[8] The stratigraphy and grain size characteristics of the Kos Plateau Tuff have been described in detail by Allen and co-workers [Allen, 2001; Allen and Cas, 2001; Allen *et al.*, 1999]. The KPT is best preserved on Kos, but also occurs on the neighboring Greek islands of Tilos, Kalymnos, Pachia, as well as on the Turkish peninsula of Bodrum and Datca (Figure 1). Isopach, isopleth and transport direction data indicate that the vent areas for the KPT were situated in the bay on the southwest part of Kos (west Kos Basin). The eruption formed a caldera at least 6–11 km in diameter. Subsequent activity such as the Nisyros composite volcano, the Yali pumice cone and rhyolitic lavas, the Pleistocene-recent Strongyle basaltic andesite cone, and several submarine volcanoes in the area of Yali and Nisyros all indicate that the Kos system remains magmatically active.



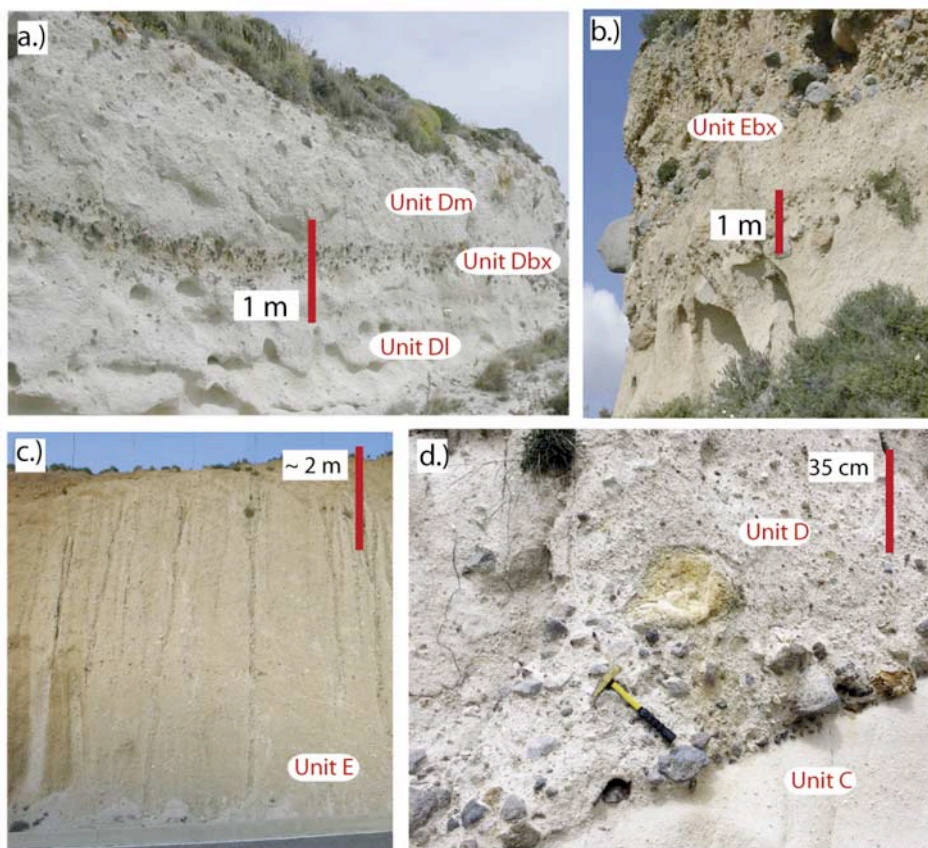


**Figure 2.** Photos of selected outcrops of the KPT showing the thickness and lithic-carrying capacity of these flows. The lithics are predominately andesitic in composition. (a) Unit Dbx is a double-layer lithic breccia separating the relatively lithic poor ignimbrites Dl and Dm (Sunny Beach, Kos). (b) Unit Ebx is a basal lithic breccia underlying E1, interpreted to be the climax of the eruption (central, Kos) [Allen *et al.*, 1999]. (c) Unit E1 on the island of Tilos. (d) Contrast between unit C and D1. C is composed of fine- and medium-grained pumice and lithic lapilli with ash-rich matrix interpreted as a pyroclastic surge deposit, and D1 is fine-poor ignimbrite with lithics >20 cm at the base at this location (Golden Beach, Kos).

[9] Six main units define the stratigraphy of the KPT [Allen, 2001]. Ignimbrite units D and E dominate, with thicknesses that range from 5 to greater than 15 m, and overlay a fall unit (A) and low-angle cross-stratified units (B and C). Unit D is about 10 km<sup>3</sup> (DRE) and consists of three ignimbrites, which extend ~39 km from the source. Unit E is more voluminous with a volume of >30 km<sup>3</sup> (DRE), is composed of two ignimbrites and is interpreted as the eruption climax. The eruption began and ended with phreato-plinian activity, but the even more explosive and caldera-forming phases (D and E) were likely a result of “dry” fragmentation based on the observation of clean (non-adhering ash) finely vesiculated tube pumices [Allen *et al.*, 1999]. The distal portions of the KPT on the Datca Peninsula, Tilos, Bodrum

and Kalymnos were deposited at similar elevations and distance from the source. Thus variations in the nature of the pyroclastic deposits can be used as a means of comparing and contrasting the mechanics and deposits to help distinguish whether flows have traveled over land or water.

[10] The distribution of lithic fragments provides a constraint on the dynamics of the large ignimbrite-producing flows (Figure 2). Most (>80%) of the lithic fragments in the KPT are andesite clasts. Since most of the exposed “bedrock” on Kos (and neighboring islands) are soft sediments and limestone, these lithics are likely derived from near the original vent (either a pre-eruptive edifice or the eruptive conduit) and are not likely picked up during transport. The maximum lithic size from

**Table 1.** Notation

Parameter	Description	Units
$\bar{c}_p$	heat capacity	J/kg K
$^p d$	particle diameter	m
$\bar{g}$	gravitational acceleration	m/s <sup>2</sup>
$\bar{H}$	mean interphase heat transfer	J/m <sup>3</sup> s
$I$	interphase momentum transfer (drag)	Pa/m <sup>3</sup>
$k$	thermal conductivity	W/m K
$m$	mass	kg
$P$	pressure	Pa
$q$	thermal heat flux	J/m <sup>2</sup> s
$T$	temperature	K
$U_i$	velocity	m/s
$\mathbf{x}$	spatial position	m
$\alpha$	volume fraction	
$\rho$	density	kg/m <sup>3</sup>
$\tau_{ij}$	stress tensor	Pa
$\theta$	granular temperature	m <sup>2</sup> /s <sup>2</sup>
$\mu$	dynamic viscosity	Pa s
$\varphi$	specularity	
$\eta$	particle number density	
$^p \text{Re}$	particle Reynolds number <sup>a</sup>	
$g_0$	radial distribution function <sup>a</sup>	

<sup>a</sup>Superscripts: *s*, particle phases; *w*, water phase; *v*, water vapor. Subscripts: *i, j* = 1, 2 (indices for spatial direction).

unit D are significantly smaller in flows that have traversed to the south, potentially as a result of lithic loss through a water boundary. Likewise the deposit thickness is much less in sections where the flow has thought to have crossed water, which may indicate that a significant amount of dense lower portion of the flow was lost during transport. This stands in contrast to the more voluminous and coarser E flows that have a fairly uniform thickness up to 40 km from the source, and have no distinguishable maximum lithic size variations between flows that have been hypothesized to cross water compared to those thought to have crossed land.

### 3. Simulation Approach and Eruption Conditions

[11] We conducted a suite of two-dimensional and three-dimensional simulations of the Kos eruption to better understand the role of the basal boundary condition on pyroclastic flow transport during moderate to large eruptive events. We incorporated both leaky and saltation boundary conditions into continuum multiphase numerical simulations, based on the MFIX (multiphase flow with interface

exchanges) approach adapted for volcanic flows [Dufek and Bergantz, 2005; Gera et al., 2004; Syamlal et al., 1993]. Both the boundary condition approach and the numerical method were validated by Dufek and Bergantz [2007] for particle-laden gravity currents, by comparing the results to direct numerical simulations and experimental results. For a detailed discussion of the continuum multiphase approach used in these simulations we refer the reader to Dufek and Bergantz [2007] that used the same approach. Similar to other continuum multiphase numerical approaches applied to volcanic conditions [Clarke et al., 2002; Darteville et al., 2004; Dufek and Bergantz, 2005; Neri et al., 2002; Todesco et al., 2006], separate continua (gas and particle) equations for mass, momentum and energy conservation are used to describe the physical system. We summarize the continua equations below. The gas and particle continuity equations are given as

$$\frac{\partial}{\partial t} (^g \alpha^g \rho) + \frac{\partial}{\partial \mathbf{x}_i} (^g \alpha^g \rho^g U_i) = 0, \quad (1)$$

and

$$\frac{\partial}{\partial t} (^s \alpha^s \rho) + \frac{\partial}{\partial \mathbf{x}_i} (^s \alpha^s \rho^s U_i) = 0, \quad (2)$$

respectively. Similarly, the momentum equations for the gas and particle phases are given as

$$\frac{\partial}{\partial t} (^g \alpha^g \rho U_i) + \frac{\partial}{\partial \mathbf{x}_i} (^g \alpha^g \rho^g U_i^g U_j) = \frac{\partial^g P}{\partial \mathbf{x}_i} \delta_{ij} + \frac{\partial^g \tau_{ij}}{\partial \mathbf{x}_j} + ^g I_i + ^g \alpha^g \rho g_i, \quad (3)$$

and

$$\frac{\partial}{\partial t} (^s \alpha^s \rho U_i) + \frac{\partial}{\partial \mathbf{x}_i} (^s \alpha^s \rho^s U_i^s U_j) = \frac{\partial^s P}{\partial \mathbf{x}_i} \delta_{ij} + \frac{\partial^s \tau_{ij}}{\partial \mathbf{x}_j} + ^s I_i + ^s \alpha^s \rho g_i. \quad (4)$$

The gas and particle phase thermal energy conservation relations are

$$^g \alpha^g \rho^g c_p \left( \frac{\partial^g T}{\partial t} + ^g U_i \frac{\partial^g T}{\partial \mathbf{x}_i} \right) = \frac{\partial^g q}{\partial \mathbf{x}_i} + \bar{H}_{gs}, \quad (5)$$

and

$$^s \alpha^s \rho^s c_p \left( \frac{\partial^s T}{\partial t} + ^s U_i \frac{\partial^s T}{\partial \mathbf{x}_i} \right) = \frac{\partial^s q}{\partial \mathbf{x}_i} - \bar{H}_{gs}. \quad (6)$$

[12] A summary of the symbols used in these equations is included in Table 1. Constitutive relations required to close the momentum and

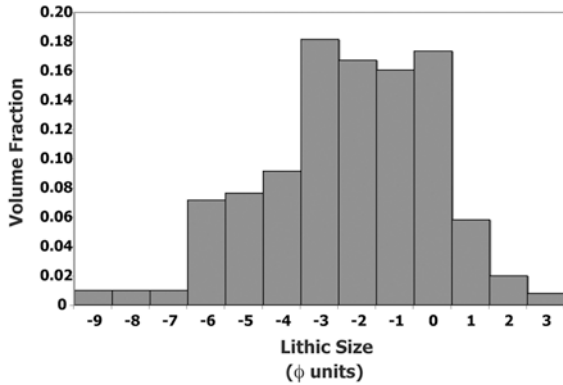


**Figure 3.** Lithic size distribution (phi units) determined from a compilation of *Allen* [2001] sieve data for ignimbrite units D and E. Sieve data encompass data  $\phi = -6$  and higher. We assume a 0.01 volume fraction for the  $\phi = -7, -8, -9$  bins, although we do not have sieve data for these size fractions. We include these size fractions on the basis of the presence of maximum lithic sizes in these ranges, and although volumetrically insignificant, we model these size fractions to compare to maximum lithic size data.

thermal energy equations are described in detail by *Dufek and Bergantz* [2007]. For collisional transfer of momentum, the constitutive relation for the particle phase is provided by kinetic theory similar to that used in the estimation of gas viscosities from molecular collisions [*Dufek and Bergantz, 2005; Lun et al., 1984*]. This constitutive relation assumes binary, inelastic particle collisions. The collision rate and stress in the granular material depends on the fluctuating particle velocity. A separate transport equation for pseudo-thermal energy is solved in order to determine the granular temperature (variance of the velocity distribution) and close the granular stress in dilute conditions. Pseudo-thermal energy is assumed to be advected by the mean flow and diffuses along gradients in the granular temperature. Locally pseudo-thermal energy is produced by shear and by the relative velocity between the particle and gas phases [*Agrawal et al., 2001*] and is dissipated by inelastic collisions and by viscous damping by the carrier fluid. The production of fluctuating motions by gas-particle slip and dissipation by viscous forces ensures that the granular pseudo-thermal energy equation is coupled to the carrier fluid. At higher particle volume fractions, protracted frictional interaction of particles occurs and the frictional and collisional stresses are assumed to be additive [*Savage, 1998; Syamlal, 1987*]. The frictional stress is developed using the postulate of a yield

function and an associated flow-rule to relate stress and strain rate, and has been adopted from theories of soil mechanics. The solids pressure in the frictional regime allows the solid phases to have some compressibility, but provides a resisting force to prevent unphysical void fractions. In the limit of volume fractions approaching the minimum void fraction both the frictional pressure and granular shear viscosity approach infinity, which prevents further circulation of material. A modified  $k-\epsilon$  turbulence model is used to predict Reynolds stresses produced by fluctuating fluid motion. This approach accounts for production and dissipation of turbulent energy due to the presence of a dispersed phase [*Peirano and Leckner, 1998*].

[13] The boundary conditions for both the saltation and the leaky (or overwater) boundaries were derived by *Dufek and Bergantz* [2007]. The saltation boundary is maintained by imposing a velocity gradient across the boundary using a ghost cell technique. The velocity gradient relation is adapted from *Johnson and Jackson* [1987] given as

$$\frac{\partial u}{\partial y} = \frac{s \alpha g_0 (3\theta)^{-5} \phi \pi^s \rho U_{slip}}{6 (s \alpha^0)^g \mu}, \quad (7)$$

where  $\phi$  is the specularity coefficient (here we specify a constant value of 0.02 based on the experimental comparison of *Benyahia et al.* [2005]) and  $U_{slip}$  is the slip velocity at the boundary. We note that natural boundaries likely display a range of roughness and corresponding specularity. The leaky boundary is derived by integrating the velocity probability distribution function of the particle phase over the time step, to determine the volume fraction of particles lost. This is given as

$$\gamma = \frac{s \alpha}{2} \left[ 1 + \operatorname{erf} \left( \frac{v_{leak} - \bar{v}}{\sqrt{2\theta}} \right) \right], \quad (8)$$

where  $\gamma$  is the volume fraction loss rate over the computational time step,  $\theta$  is the granular temperature,  $v_{leak}$  is the velocity sufficient to remove a particle from a given height in the flow during a time interval ( $v_{leak} = \frac{l}{\Delta t}$ ),  $\bar{v}$  is the average vertical velocity, and erf is the error function.

[14] We simulated two continua (gas and particles) and in sub-set of numerical models we also explicitly included particle-tracking (Lagrangian particles) with initial size distributions determined from a compilation of the grain size distributions for units D and E of the KPT (Figure 3). While the



instantaneous lithic size distribution from the vent likely varies from this distribution, the maximum grain size versus distance from the vent is relatively insensitive to the precise distribution provided that the dominant grain sizes are represented, although predicted distributions in the deposit are sensitive to the source distribution. The small diameter particles represented in the continuum portions of the simulations had a diameter of 250  $\mu\text{m}$ .

[15] The Lagrangian particles are coupled with the gas and particle continua through drag terms using an approach proposed by *Fan et al.* [2000]. In this Eulerian-Eulerian-Lagrangian (EEL) approach the Lagrangian particles are one-way coupled to both the particulate (solid) continua and the gas continua, which is appropriate for the distinctive, but volumetrically minor lithic clasts of the KPT. In the following set of equations (and in the prior continua relations) the superscript “p” refers to Lagrangian particles, “s” refers to the solid particle continua, and “g” refers to the gas continua.

[16] The Lagrangian equation of motion is given as

$$\frac{\partial^p u_i}{\partial t} = -\frac{1}{\rho_p} \frac{\partial^g P}{\partial x_i} - \frac{1}{\rho_p} \frac{\partial^s P}{\partial x_i} + \frac{{}^{gp}F_d}{m_p} + \frac{{}^{sp}F_d}{m_p} + \mathbf{g}, \quad (9)$$

where  $m_p$  is the mass of the Lagrangian particle,  ${}^p u_i$  is the particle velocity,  $\rho_p$  is the particle density,  ${}^g P$  and  ${}^s P$  are the pressures of the gas and solid continua, respectively, and  ${}^{gp}F_d$  and  ${}^{sp}F_d$  are the drag forces between the Lagrangian particle and the gas and solid continua, respectively. As the particle density is much greater than the gas density, the pressure gradient terms have minor influence on the particle path relative to the drag forces and gravity [*Fan et al.*, 2000]. The gas-particle drag force is given as

$${}^{gp}F_d = \frac{\beta_f [{}^g u_i - {}^p u_i]}{s \alpha \eta}, \quad (10)$$

where the drag coefficient is given as

$$\beta_f = \frac{0.75 C_d s \alpha (1 - s \alpha)^g \rho [{}^g u_i - {}^p u_i] s \alpha^{-2.65}}{s d}, \quad (11)$$

and

$$C_d = \begin{cases} \frac{24 [1 + 0.15 \text{Re}_p^{0.68}]}{\text{Re}_p}, & \text{Re}_p < 1000 \\ 0.44, & \text{Re}_p \geq 1000 \end{cases}. \quad (12)$$

The solid continua-particle drag is given as

$${}^{sp}F_d = \frac{m_p [{}^s u_i - {}^p u_i] g_0}{\delta}, \quad (13)$$

where  $g_0$  is the dimensionless radial distribution function and  $\delta$  is the mean inter-particle collision time given as

$$\delta = \frac{0.0904 d_p}{s \alpha g_0 \sqrt{s \theta}}. \quad (14)$$

The radial distribution function approaches large values as the solid volume fraction approaches close packing. In situations with either high granular temperature or as close packing is approached, the mean inter-particle collision time decreases; this intuitively results in very large values of the particle-solid drag force, so that the Lagrangian particles accelerate rapidly to match the solid continua velocity in these situations. This ultimately results in the deposition of the Lagrangian particles in regions of the flow that reach close packing and have zero solid continua velocity.

[17] The two-dimensional simulations have topography sampled from the dashed lines in Figure 1, for both simulation sections 1 (north toward Kalymnos) and 2 (south toward Tilos). Three-dimensional simulations were conducted in cylindrical coordinates in the arcs demarked on Figure 1. Vertical resolution was refined near the boundary going from 10 m near the boundary to 100 m near the top of the simulations. Horizontal resolution was refined near areas of topography with minimum and maximum resolution of 20 m and 100 m. The top and side boundary conditions were outflow boundaries. The ambient atmosphere was taken as the U.S. standard atmosphere [*National Oceanic and Atmospheric Administration*, 1976] with the tropopause at 11 km.

#### 4. Constraints on Eruptive Geometry and Intensity

[18] The exact eruptive geometry at the time of the eruption of the KPT is unknown. Allen et al. suggested that the eruption may have evolved from an early central vent mode of eruption to ring dike and caldera collapse style of eruption [*Allen et al.*, 1999]. However, the nature of the caldera collapse style of eruption obscures prior vent conditions and hence we have treated vent geometry as a free

**Table 2.** Simulation Conditions

Simulation Number	Vent Type <sup>a</sup>	Vent Area, m <sup>2</sup>	Volume Fraction Particles	Vent Velocity, m/s	Temp., K	Eruptive Flux, m <sup>3</sup> /s	Collapse?
1_100	CV	3.14 × 10 <sup>4</sup>	0.04	41.6	950	5.22 × 10 <sup>4</sup>	Y
2_100	CV	3.14 × 10 <sup>4</sup>	0.03	47.7	950	4.49 × 10 <sup>4</sup>	Y
3_100	CV	3.14 × 10 <sup>4</sup>	0.02	58.1	950	3.65 × 10 <sup>4</sup>	Y
4_100	CV	3.14 × 10 <sup>4</sup>	0.015	66.8	950	3.15 × 10 <sup>4</sup>	Y
5_100	CV	3.14 × 10 <sup>4</sup>	0.005	114.0	950	1.79 × 10 <sup>4</sup>	Y
6_100	CV	3.14 × 10 <sup>4</sup>	0.002	176.2	950	1.11 × 10 <sup>4</sup>	Y
7_100	CV	3.14 × 10 <sup>4</sup>	0.0015	201.0	950	9.47 × 10 <sup>3</sup>	N
8_100	CV	3.14 × 10 <sup>4</sup>	0.0012	222.2	950	8.37 × 10 <sup>3</sup>	N
9_100	CV	3.14 × 10 <sup>4</sup>	0.0009	235.8	950	6.66 × 10 <sup>3</sup>	N
10_100	CV	3.14 × 10 <sup>4</sup>	0.0008	264.7	950	6.65 × 10 <sup>3</sup>	N
1_200	CV	1.26 × 10 <sup>5</sup>	0.04	41.6	950	2.08 × 10 <sup>5</sup>	Y
2_200	CV	1.26 × 10 <sup>5</sup>	0.03	47.7	950	1.80 × 10 <sup>5</sup>	Y
3_200	CV	1.26 × 10 <sup>5</sup>	0.02	58.1	950	1.45 × 10 <sup>5</sup>	Y
4_200	CV	1.26 × 10 <sup>5</sup>	0.015	66.8	950	1.26 × 10 <sup>5</sup>	Y
5_200	CV	1.26 × 10 <sup>5</sup>	0.005	114.0	950	7.16 × 10 <sup>4</sup>	Y
6_200	CV	1.26 × 10 <sup>5</sup>	0.002	176.2	950	4.43 × 10 <sup>4</sup>	Y
7_200	CV	1.26 × 10 <sup>5</sup>	0.0015	201.0	950	3.79 × 10 <sup>4</sup>	Y
8_200	CV	1.26 × 10 <sup>5</sup>	0.0012	222.2	950	3.35 × 10 <sup>4</sup>	Y
9_200	CV	1.26 × 10 <sup>5</sup>	0.0009	235.8	950	2.67 × 10 <sup>4</sup>	N
10_200	CV	1.26 × 10 <sup>5</sup>	0.0008	264.7	950	2.66 × 10 <sup>4</sup>	N
1_400	CV	5.02 × 10 <sup>5</sup>	0.04	41.6	950	8.36 × 10 <sup>5</sup>	Y
2_400	CV	5.02 × 10 <sup>5</sup>	0.03	47.7	950	7.20 × 10 <sup>5</sup>	Y
3_400	CV	5.02 × 10 <sup>5</sup>	0.02	58.1	950	5.84 × 10 <sup>5</sup>	Y
4_400	CV	5.02 × 10 <sup>5</sup>	0.015	66.8	950	5.03 × 10 <sup>5</sup>	Y
5_400	CV	5.02 × 10 <sup>5</sup>	0.005	114.0	950	2.86 × 10 <sup>5</sup>	Y
6_400	CV	5.02 × 10 <sup>5</sup>	0.002	176.2	950	1.77 × 10 <sup>5</sup>	Y
7_400	CV	5.02 × 10 <sup>5</sup>	0.0015	201.0	950	1.51 × 10 <sup>5</sup>	Y
8_400	CV	5.02 × 10 <sup>5</sup>	0.0012	222.2	950	1.34 × 10 <sup>5</sup>	Y
9_400	CV	5.02 × 10 <sup>5</sup>	0.0009	235.8	950	1.07 × 10 <sup>5</sup>	Y
10_400	CV	5.02 × 10 <sup>5</sup>	0.0008	264.7	950	1.06 × 10 <sup>5</sup>	Y
1_200RV	RV	6.28 × 10 <sup>6</sup>	0.04	41.6	950	1.04 × 10 <sup>7</sup>	Y
2_200RV	RV	6.28 × 10 <sup>6</sup>	0.03	47.7	950	8.98 × 10 <sup>6</sup>	Y
3_200RV	RV	6.28 × 10 <sup>6</sup>	0.02	58.1	950	7.28 × 10 <sup>6</sup>	Y
4_200RV	RV	6.28 × 10 <sup>6</sup>	0.015	66.8	950	6.31 × 10 <sup>6</sup>	Y
5_200RV	RV	6.28 × 10 <sup>6</sup>	0.005	114.0	950	3.58 × 10 <sup>6</sup>	Y
6_200RV	RV	6.28 × 10 <sup>6</sup>	0.002	176.2	950	2.21 × 10 <sup>6</sup>	Y
7_200RV	RV	6.28 × 10 <sup>6</sup>	0.0015	201.0	950	1.89 × 10 <sup>6</sup>	Y
8_200RV	RV	6.28 × 10 <sup>6</sup>	0.0012	222.2	950	1.67 × 10 <sup>6</sup>	Y
9_200RV	RV	6.28 × 10 <sup>6</sup>	0.0009	235.8	950	1.33 × 10 <sup>6</sup>	N
10_200RV	RV	6.28 × 10 <sup>6</sup>	0.0008	264.7	950	1.32 × 10 <sup>6</sup>	N
1_200RV_P1	RV	6.28 × 10 <sup>6</sup>	0.04	56.6	950	1.45 × 10 <sup>7</sup>	Y
2_200RV_P1	RV	6.28 × 10 <sup>6</sup>	0.03	60.6	950	1.16 × 10 <sup>7</sup>	Y
3_200RV_P1	RV	6.28 × 10 <sup>6</sup>	0.02	68.6	950	8.78 × 10 <sup>6</sup>	Y
4_200RV_P1	RV	6.28 × 10 <sup>6</sup>	0.015	75.9	950	7.28 × 10 <sup>6</sup>	Y
5_200RV_P1	RV	6.28 × 10 <sup>6</sup>	0.005	119.2	950	3.81 × 10 <sup>6</sup>	Y
6_200RV_P1	RV	6.28 × 10 <sup>6</sup>	0.002	179.4	950	2.29 × 10 <sup>6</sup>	Y
7_200RV_P1	RV	6.28 × 10 <sup>6</sup>	0.0015	203.8	950	1.95 × 10 <sup>6</sup>	Y
8_200RV_P1	RV	6.28 × 10 <sup>6</sup>	0.0012	224.6	950	1.73 × 10 <sup>6</sup>	Y
9_200RV_P1	RV	6.28 × 10 <sup>6</sup>	0.0009	253.9	950	1.46 × 10 <sup>6</sup>	N
10_200RV_P1	RV	6.28 × 10 <sup>6</sup>	0.0008	266.6	950	1.37 × 10 <sup>6</sup>	N
1_200RV_P2	RV	6.28 × 10 <sup>6</sup>	0.04	123.1	950	3.15 × 10 <sup>7</sup>	Y
2_200RV_P2	RV	6.28 × 10 <sup>6</sup>	0.03	117.9	950	2.27 × 10 <sup>7</sup>	Y
3_200RV_P2	RV	6.28 × 10 <sup>6</sup>	0.02	115.0	950	1.47 × 10 <sup>7</sup>	Y
4_200RV_P2	RV	6.28 × 10 <sup>6</sup>	0.015	115.9	950	1.11 × 10 <sup>7</sup>	Y
5_200RV_P2	RV	6.28 × 10 <sup>6</sup>	0.005	141.9	950	4.55 × 10 <sup>6</sup>	Y
6_200RV_P2	RV	6.28 × 10 <sup>6</sup>	0.002	193.5	950	2.47 × 10 <sup>6</sup>	Y
7_200RV_P2	RV	6.28 × 10 <sup>6</sup>	0.0015	215.8	950	2.07 × 10 <sup>6</sup>	Y
8_200RV_P2	RV	6.28 × 10 <sup>6</sup>	0.0012	235.3	950	1.81 × 10 <sup>6</sup>	Y
9_200RV_P2	RV	6.28 × 10 <sup>6</sup>	0.0009	263.0	950	1.52 × 10 <sup>6</sup>	N
10_200RV_P2	RV	6.28 × 10 <sup>6</sup>	0.0008	275.1	950	1.37 × 10 <sup>6</sup>	N
1_200RV_P3	RV	6.28 × 10 <sup>6</sup>	0.04	206.3	950	5.28 × 10 <sup>7</sup>	Y



**Table 2.** (continued)

Simulation Number	Vent Type <sup>a</sup>	Vent Area, m <sup>2</sup>	Volume Fraction Particles	Vent Velocity, m/s	Temp., K	Eruptive Flux, m <sup>3</sup> /s	Collapse?
2_200RV_P3	RV	$6.28 \times 10^6$	0.03	189.6	950	$3.64 \times 10^7$	Y
3_200RV_P3	RV	$6.28 \times 10^6$	0.02	173.1	950	$2.21 \times 10^7$	Y
4_200RV_P3	RV	$6.28 \times 10^6$	0.015	166.1	950	$1.59 \times 10^7$	Y
5_200RV_P3	RV	$6.28 \times 10^6$	0.005	170.5	950	$5.46 \times 10^6$	Y
6_200RV_P3	RV	$6.28 \times 10^6$	0.002	211.1	950	$2.79 \times 10^6$	Y
7_200RV_P3	RV	$6.28 \times 10^6$	0.0015	230.9	950	$2.21 \times 10^6$	Y
8_200RV_P3	RV	$6.28 \times 10^6$	0.0012	248.6	950	$1.91 \times 10^6$	N
9_200RV_P3	RV	$6.28 \times 10^6$	0.0009	274.3	950	$1.58 \times 10^6$	N
10_200RV_P3	RV	$6.28 \times 10^6$	0.0008	285.7	950	$1.46 \times 10^6$	N

<sup>a</sup>CV denotes central vent, and RV denotes ring vent. The ring vent simulations were conducted at a radius of 5 km, and were 200 m wide. Simulation numbers with the suffix “\_P1” refer to a vent overpressure of  $10^6$  Pa, those with “\_P2” refer to an overpressure of  $5 \times 10^6$  Pa, and those with “\_P3” refer to an overpressure of  $10^7$  Pa. Simulation numbers without the “\_P” suffix are pressure-balanced.

parameter to explore the style and flux generated from a number of scenarios from central vent to ring dike geometries. We surveyed the sensitivity of vent geometries and vent particle flux using two-dimensional simulations as summarized in Table 2. Central vent radii of 100 m, 200 m and 400 m were considered, as was a ring vent structure with a radius of 5 km, similar to the inferred radius of the Kos Plateau Tuff caldera. Vent velocities were determined using a choked flow constraint [Papale and Dobran, 1994]; i.e., if vent geometry is static the speed achieved at the opening of the conduit will be the speed of sound of the particle-laden gas. We considered both pressure-balanced and overpressure conditions at the vent. We approximate the speed of sound of the mixture

coming out of the vent by assuming the mixture is initially isothermal [Dobran, 2001]. By imposing choked flow, the highest flux of particles occurs at lower exit velocities (but greater particle volume fraction). We stress that these simulations were intended to test the sensitivity of the resulting pyroclastic flows on vent conditions and topography, and due to the necessary simplifications in vent geometry and the choked flow assumption we are more interested in the general and robust trends rather than detailed comparison.

[19] The two-dimensional simulations can be broadly grouped into three categories: (1) boiling-over regime, (2) collapsing column regime, and (3) plinian column regime. Examples of the three

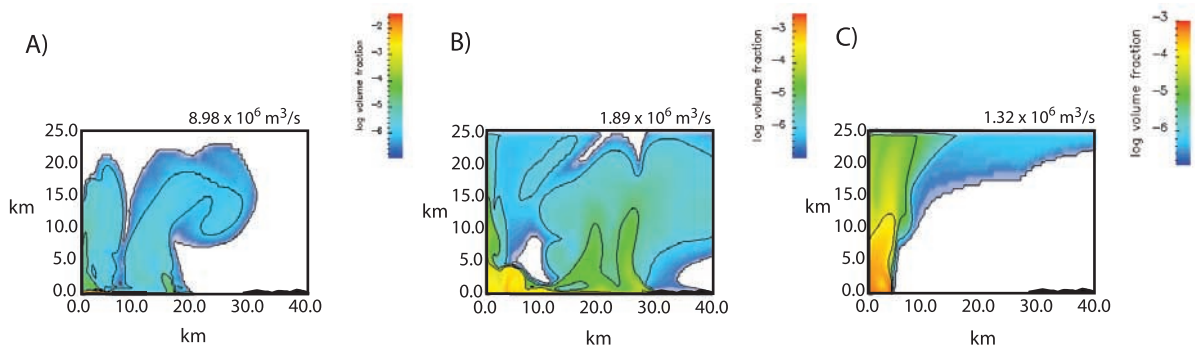


**Figure 4.** Volume fraction of particles at 1000 s for three different eruptive fluxes of (a)  $8.98 \times 10^6$  m<sup>3</sup>/s, (b)  $1.89 \times 10^6$  m<sup>3</sup>/s, and (c)  $1.32 \times 10^6$  m<sup>3</sup>/s. Scale is in kilometers. Simulations shown in this figure have a ring vent geometry, with the vent location having a radius of 5 km and a width of 200 m. Figure 4a shows a typical boiling-over style of eruption, which initially has very small column height and produces dense pyroclastic density currents. The relatively low velocity out of the vent (47.7 m/s) of this current results in early sedimentation of particles, comparatively small runout distances, and secondary plumes. Figure 4b shows column collapse eruption with resulting pyroclastic density current. For the same vent geometry these events are generated by a higher-velocity gas-particle mixture at the vent compared to the boiling-over flows but are more particle dilute. Even though they have comparatively small volume flux of particles, they produce pyroclastic density currents with much greater runout distances. As shown in Figure 4c, at still smaller volume flux of particles the very high velocity of the gas-particle mixture ascends in a buoyant plume, rising into the stratosphere.

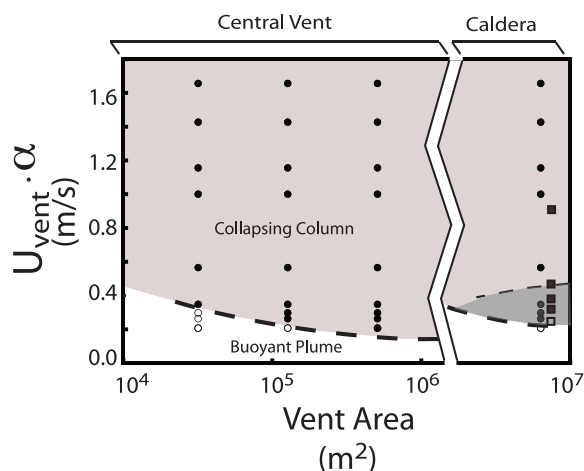


**Figure 5.** Regime diagram for eruptive behavior. Dark circles denote simulations in which the eruptive column partially or completely collapsed, and open circles denote stable buoyant plinian eruptions. Light grey shading denotes the field of collapsing columns. Squares symbols denote overpressurized vent conditions;  $P = 10^7$  Pa (only a subset of simulations are included in the figure for clarity). Central vent and ring fracture geometries are shown in separate fields. The dark grey shading marks the simulated conditions, which not only produced collapsing columns with pyroclastic density currents but also had the mobility to reach the islands of Kalymnos and Tilos in the simulations, comparable with range of the KPT deposits.

eruptive styles are shown in Figure 4. The boiling-over regime is characterized by very high volume flux out of the vent, but low eruptive velocities. The boiling-over events are really a type of column collapse event where the columns are dense enough that the initial column heights are small ( $<10\%$  the tropopause height) and form dense, ground-hugging gravity currents. The height of the initial column of material is typically restricted to less than a few kilometers, and rapid deposition generates thick and poorly sorted deposits within 10–20 km from the vent. The rapid loss of material to deposition typically generates buoyant secondary columns (typically referred to as phoenix columns or co-ignimbrite clouds) as shown in Figure 4a [Giordano and Dobran, 1994]. While these simulated flows easily surmounted the low-lying topography of Kos, even for the ring vent structure (which maximizes vent area) the boiling-over events failed to have long enough runout to reach or surmount topography at Kalymnos as observed for the Vathi Valley deposits in north-eastern Kalymnos.

[20] By comparison the collapsing column events have lower flux than the boiling-over counterparts, but have much greater vent velocities. However, even with these higher vent velocities, the collapsing column regime produced from a central vent failed to reach and surmount topography at Kalymnos. Only the larger ring fracture collapsing column events (as shown in Figure 4b) reached and surmounted some of the topography at Kalymnos. Secondary buoyant columns are generated as material is deposited. Where flows encounter steep topography, with subsequent rapid deposition, the phoenix columns are strongly correlated with topographic roughness.

[21] At still greater vent velocities (and more dilute flow), buoyant plinian columns are generated, both from central vents and ring vents. The majority of the particulate material is carried upward to the stratosphere where it spreads forming large plumes that eventually exceed the range of the simulated domain ( $>50$  km).

[22] Figure 5 summarizes the results of the two-dimensional simulations. The black (filled-in) symbols denote simulations with column collapse, and the open symbols denote stable plinian events. The central vent and caldera (ring fracture) fields are separated by the gap in Figure 5, with ring fracture events having much greater total vent area. A further field is shown (dark gray) where the simulations produced pyroclastic flows that reach the valleys of Kalymnos as is observed in deposits of the KPT. The overpressurized vent conditions extend the range of collapsing columns and flow run-out distances that reach Kalymnos to higher particle volume flux (Table 2 and Figure 5). We primarily focus the three-dimensional investigation on the eruptive conditions that reach Kalymnos to further assess the topographically controlled behavior of the pyroclastic flows generated by these conditions as well as the influence of overwater transit.

## 5. Topographic and Boundary Condition Controls on Kos Plateau Tuff Dispersal

[23] The sensitivity of pyroclastic flows to boundary conditions is assessed in detail with three-dimensional simulations. We extend these calculations to three-dimensions primarily because the deposits of the KPT are controlled by topography, and in many cases are valley-fill deposits. (This is particularly true in the Vathi deposits on the island of Kalymnos,

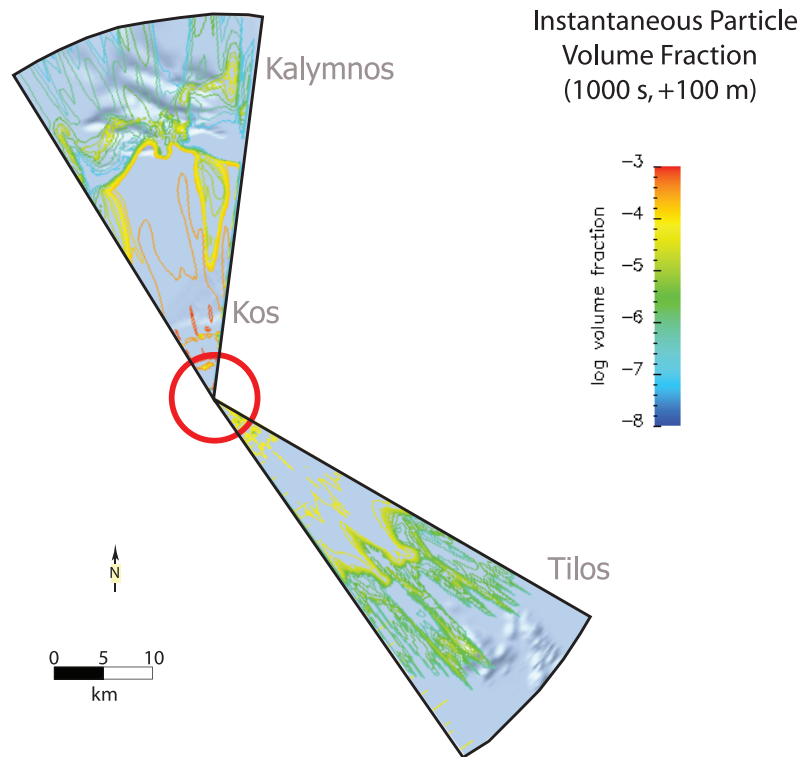


**Figure 6.** Volume fraction of particles 100 m above the surface at 1000 s for ring vent geometry and volume flux of  $1.89 \times 10^6 \text{ m}^3/\text{s}$ . Red circle denotes vent location. Flows to the south, with leaky boundaries, are more dilute than flows to the north. Radial variability in particle volume fraction occurs not only in response to topography but also due to unsteadiness of the eruptive column.

Figure 1). However, while both leaky/saltation and topographic boundary effects contribute to the spatial variability in particle concentration, there are three-dimensional instabilities, independent of conditions at the boundary that produce spatio-temporal variability. The unsteadiness of three-dimensional eruptive columns results in regions of preferential downwelling, and variability in the particle concentration at similar radial distances from the vent as measured 100 m above the surface (Figure 6). The location of preferential downwelling migrates radially during the course of the simulated eruption.

[24] After the collapse of the eruptive column, the particle-laden gravity currents initially have similar particle concentrations compared to the two-dimensional simulations with the same eruptive conditions. However, flows that traverse leaky boundaries become significantly more dilute and fail to produce a concentrated bed load region. This ultimately results in the earlier production of secondary columns (Figures 7, 8, 9, and 10). For flux conditions near  $1.9 \times 10^6 \text{ m}^3/\text{s}$  from a ring vent structure, the dominant secondary plumes are

located between 20–25 km from the vent, or about 5–10 km offshore from the island of Tilos. A series of smaller buoyant plumes are produced when the pyroclastic flow heads interact with topography at Tilos. Interestingly, bed load conditions (albeit at lower particle concentrations than their entirely overland counterparts) reform as the flows pass from leaky to saltation boundaries [Dufek and Bergantz, 2007]. Again, the eruptive fluxes less than  $\sim 1.9 \times 10^6 \text{ m}^3/\text{s}$ , due to smaller vent area, fail to produce flows that completely traverse the leaky boundary to reach Tilos. Flows with between  $1.9 \times 10^6$  to  $3.58 \times 10^6 \text{ m}^3/\text{s}$  eruptive flux reach Tilos, but are approximately 10% the concentration of their counterparts that traveled over saltation boundaries to reach Kalymnos, with typical pyroclastic head volume fractions at 100 m above the surface of less than  $1.0 \times 10^{-4}$  volume fraction (Figure 6).

[25] The three-dimensional simulations illustrate the control of topography on the pyroclastic flow concentration and deposition, as well as the location of secondary plumes (Animation 1). The most dramatic instance of this is in the case of flows that



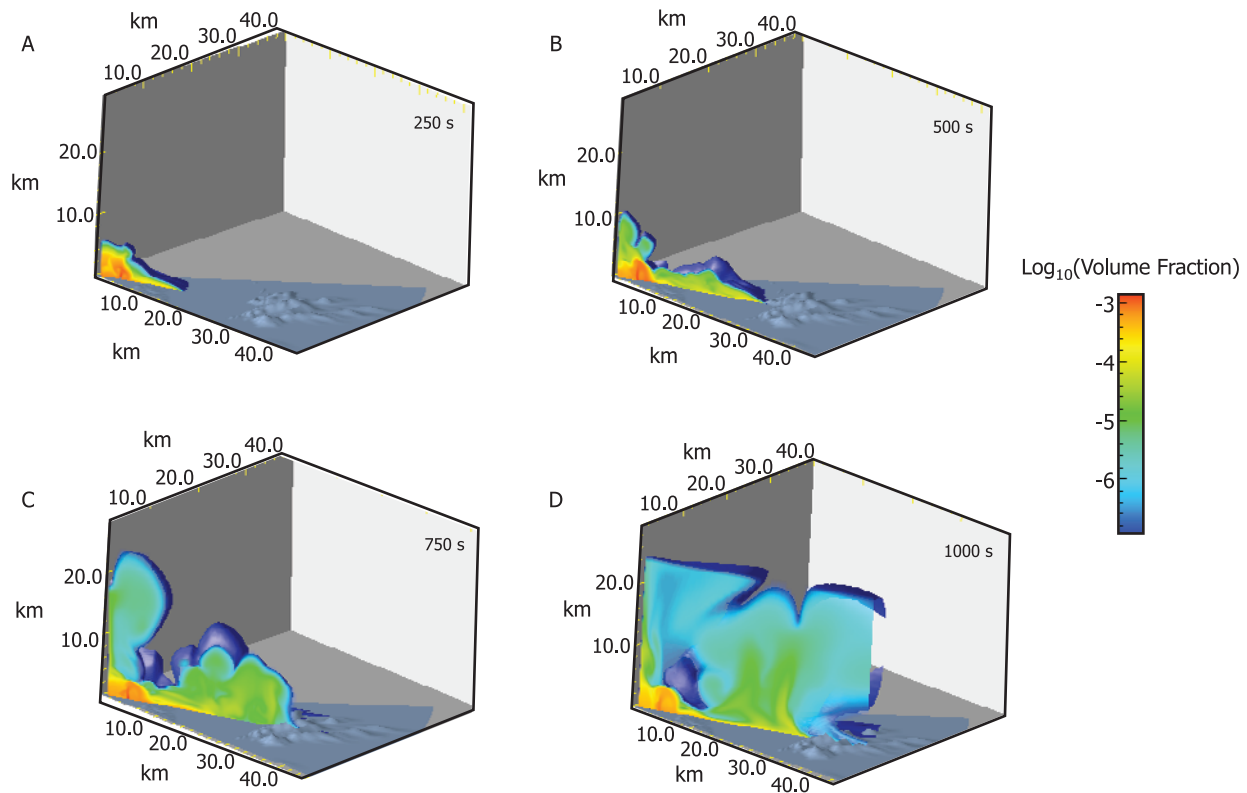


**Figure 7.** Cross section of volume fraction of particles for ring vent geometry eruption with eruptive flux of  $1.89 \times 10^6 \text{ m}^3/\text{s}$  (saltation boundary simulation, topography conditions (1) in Figure 1, flows going toward Kalymnos). Figures 7a–7d are a time sequence in 250 s intervals. The bases of saltation boundary flows are typically an order of magnitude more particle dense than their leaky boundary counterparts. The dominant secondary plumes are generated when the pyroclastic density currents encounter topography, near Kalymnos. The phoenix plumes rise to the tropopause and spread in the stratosphere. An animation of this simulation is available as dynamic content (see Animation 1).

pond in the Vathi Valley on Kalymnos (Figure 1). In this instance, a narrow valley at nearly right angles to the flow deflects a portion of the flow, which proceeds up the valley reaching 200 m elevation. A smaller, more dilute, fraction of erupted material also reaches the valley due to recirculating currents caused by a phoenix column that is generated as the pyroclastic flows encounter the steep ridges on Kalymnos (Figure 7). This is just one example where three-dimensional topography produces multiple flow types converging at single location for overlapping periods of time.

## 6. Can Suspension Overwater Explain Distal Kos Plateau Tuff to the South of the Caldera?

[26] The simulations indicate that suspension-driven flows with a volume flux of particles of approximately  $2 \times 10^6 \text{ m}^3/\text{s}$  from a ring vent

configuration could reach the island of Tilos from a caldera near Kos, even if they were separated by a large body of water. However, the ability to cross this expanse of water does not necessarily imply that the overriding current could support the large lithic clasts found even in the distal KPT on Tilos, particularly in unit E. In order to evaluate the carrying capacity of these flows for larger and denser particles we used a Lagrangian approach to track individual particles (Figure 11). Particles were seeded into the flow at the vent, consistent with a conduit origin for the dominantly andesitic lithic clasts found in the KPT, and the size distribution was governed by the compilation of grain sizes in Figure 3. An example of such a simulation, shown in Figure 11, displays the particles being dominantly concentrated in the recirculating zone near the ring vent and in the inter-caldera region. A smaller population of particles travels with the propagating pyroclastic density current, with a

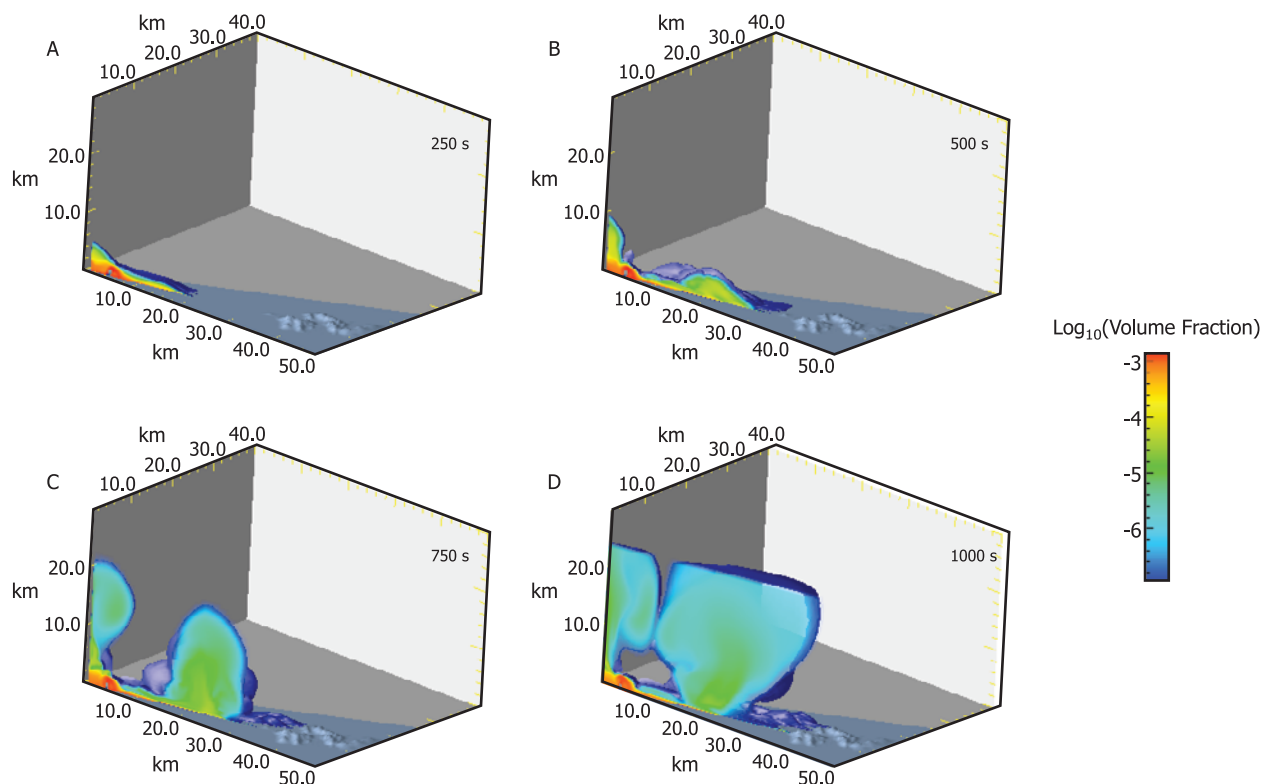


**Figure 8.** Cross section of volume fraction of particles for ring vent geometry eruption with eruptive flux of  $1.89 \times 10^6 \text{ m}^3/\text{s}$  (leaky boundary simulation, topography conditions (2) in Figure 1, flows going toward Tilos). Figures 8a–8d are a time sequence in 250 s intervals. The leaky boundary flows are significantly more dilute than the saltation boundary condition counterparts. The dominant phoenix plumes are generated 15–20 km from the vent and off the coast of Tilos, and are generated due to loss of particles through the bottom boundary.

greater volume of particles (and larger particles) concentrated at the base of the flow.

[27] From the Lagrangian simulations a synthetic maximum lithic distribution can be produced and compared to grain size data from the KPT deposit [Allen and Cas, 2001; Savage, 1998]. Figure 12b shows the synthetic maximum andesite lithic clasts for an eruptive flux of  $1.89 \times 10^6 \text{ m}^3/\text{s}$  from a ring vent configuration as described earlier. For comparison a map of the maximum lithic size distribution for unit E is shown in Figure 12a. Figure 12c shows the mean maximum lithic size versus distance from the vent (solid line) compared to maximum lithic size in both unit D and E versus distance from vent. The lithic size data are shown with 5 km error bars as the precise location of the vent/vents where these lithics were introduced into the flow is poorly constrained.

[28] The saltation (overland) simulations are able to reproduce most of the broad features of the maximum lithic size for flows that traveled to the north of the vent within error of vent uncertainty.

Larger lithics are transported in these flows in dense bed load regions where particle-particle interaction dominates momentum transfer, and particles can make multiple contacts with the bed. While the much smaller maximum lithic size distribution of unit D is similar to the leaky (overwater) simulations, these same simulations fail to account for some of the larger maximum lithic clasts found in the later unit E on the island on Tilos, even with uncertainty in vent location.

[29] The simulations indicate that in the limit of only suspension-driven transport, including drag from particle-particle collisions, pyroclastic density currents cannot transport the largest of the lithics observed in unit E on Tilos. While eruptive flux could be increased by assuming greater vent area (as for instance might occur if the caldera collapse was piecemeal), the choked flow constraint places a significant limit on lithic velocity exiting the vent, and ballistic trajectories cannot account for the transport over 30 km. A similar result also applies to increasing the ring vent radius. However,

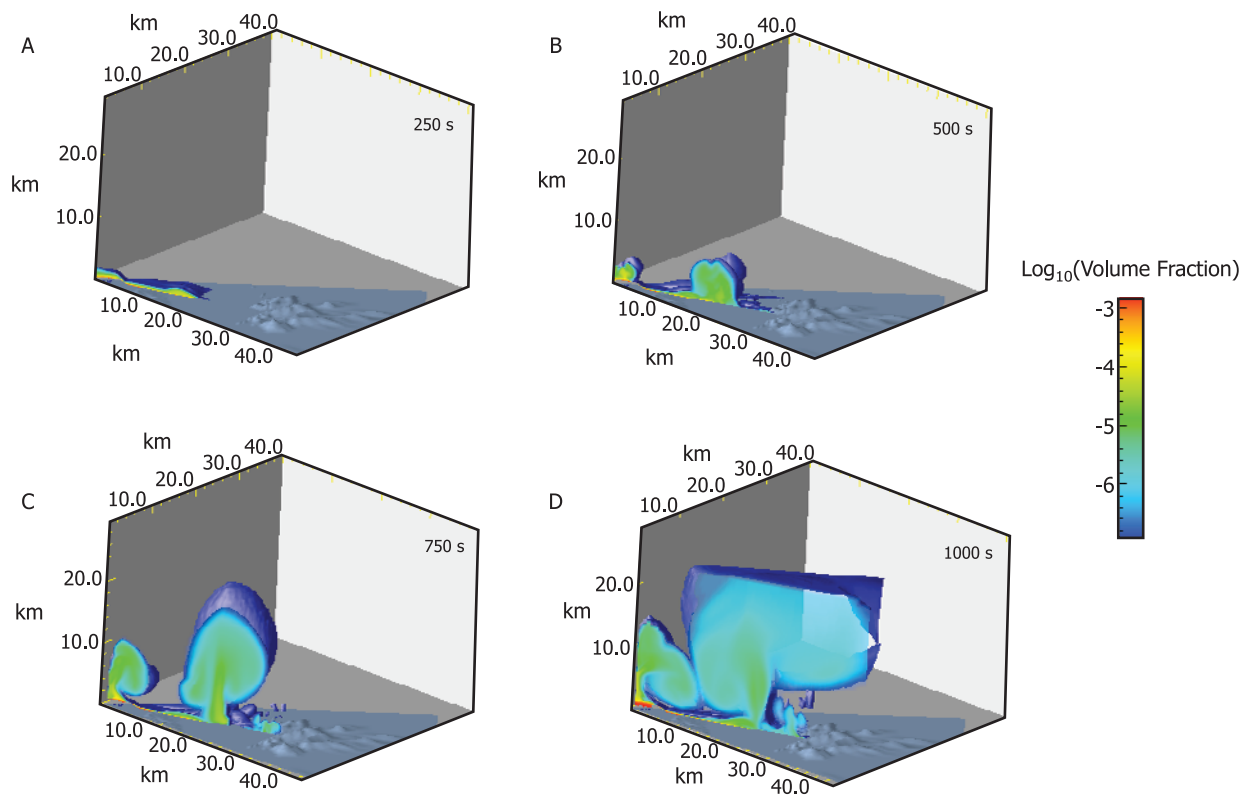


**Figure 9.** Cross section of volume fraction of particles for ring vent geometry eruption with eruptive flux of  $3.58 \times 10^6 \text{ m}^3/\text{s}$  (saltation boundary simulation, topography conditions (1) in Figure 1, flows going toward Kalymnos). Figures 9a–9d are a time sequence in 250 s intervals. The  $3.58 \times 10^6 \text{ m}^3/\text{s}$  particle volume flux was the highest flux for the ring fracture configuration that was able to reach range of the KPT deposits. It is less energetic and expanded than  $1.89 \times 10^6 \text{ m}^3/\text{s}$  flux conditions due the smaller vent velocity, and forms phoenix columns closer to the vent.

the decay of maximum particle size with distance from the vent in unit D does approach that which would be predicted from suspension-driven gravity currents including particle-particle momentum transfer.

[30] One explanation for the large lithics being transported in unit E is that the pyroclastic density current traveled mostly above a land surface that permitted saltation as suggested as one implication of the neotectonics reconstruction of Pe-Piper and coworkers [Pe-Piper *et al.*, 2005]. However, this does not explain the decay of maximum lithics from the source as seen in unit D. This decay suggests that at the start of ignimbrite producing sequence, the boundary was leaky and some depth of water was present. In the simulations we were also assuming the end-member condition of perfectly leaky boundaries; e.g., any particle that reaches the water surface is removed from the flow. One possibility is that particles can bounce to some degree across the water surface. While this

process is likely to occur, partially skipping lithics still does not explain the contrast between unit D and E (i.e., if the flows crossed water during the entirety of the eruption one would expect bouncing particles in D and E to behave similarly, and not generate the observable differences).

[31] Another alternative is that the sea was shallow and that the eruption of the preceding units of the KPT essentially filled in the depression so that the boundary evolved from leaky to saltation dominated. A similar behavior may occur as a pumice raft develops on the water surface [Allen and Cas, 2001; Carey *et al.*, 1996]. Most of the KPT pumice are at or less than the density of water, and when cooled to less than  $\sim 200^\circ\text{C}$  would be expected to remain at the water surface for days to weeks [Dufek *et al.*, 2007; Whitham and Sparks, 1986]. At the time of the eruption of unit E, much of water surface could have been covered with a pumice raft (from unit D) in excess of several meters which



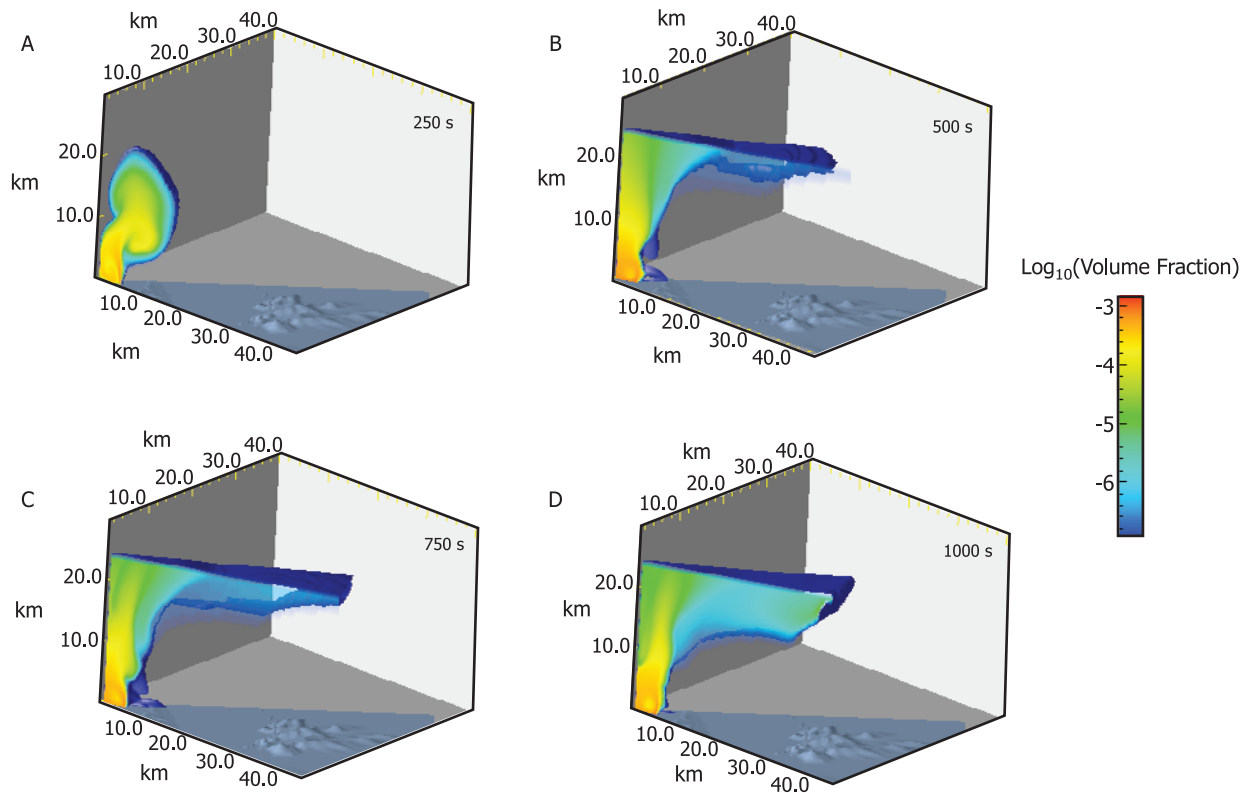


**Figure 10.** Cross section of volume fraction of particles for ring vent geometry eruption with eruptive flux of  $1.33 \times 10^6 \text{ m}^3/\text{s}$  (saltation boundary simulation, topography conditions (1) in Figure 1, flows going toward Kalymnos). Figures 10a–10d are a time sequence in 250 s intervals. The  $1.33 \times 10^6 \text{ m}^3/\text{s}$  particle volume flux was the highest flux for the ring fracture configuration that failed to produce a collapsing column.

may have served as saltation surface, which is a hypothesis that we are continuing to investigate.

## 7. Conclusions and Implications

[32] Eruption from ring vents with an eruptive flux between  $\sim 1.8 \times 10^6 \text{ m}^3/\text{s}$  to  $3.6 \times 10^6 \text{ m}^3/\text{s}$  most closely matches the implied mobility of KPT flows from the depositional distribution. Increasing the eruptive flux by increasing the vent area can explain similar mobility; however, increasing the flux through greater particle density coming out of the vent fails to produce pyroclastic density currents that reach the known deposit distribution of the KPT. Likewise smaller flux conditions and central vent configurations fail to produce flows that match the distribution of the KPT.

[33] These flux conditions permit an estimation of the eruptive duration of this moderate volume eruption (Figure 13). Using the  $60 \text{ km}^3$  volume estimate and an eruption flux of around  $2 \times 10^6 \text{ m}^3/\text{s}$  yields eruptive durations of around 0.35 days. Using the range of fluxes that produced similar

coverage as the KPT deposits gives minimum eruption duration from several hours to a couple of days. As vent overpressure is increased the apparent eruption duration timescale becomes even

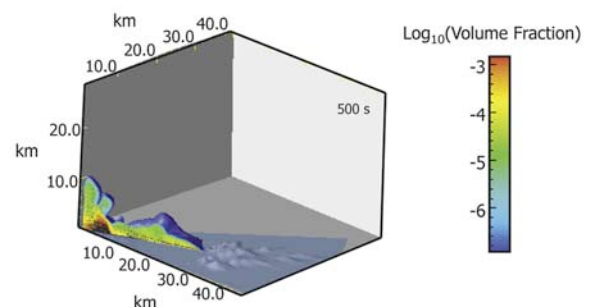


**Figure 11.** Eulerian-Eulerian-Lagrangian (EEL) simulation with volume flux of  $1.89 \times 10^6 \text{ m}^3/\text{s}$  and ring vent geometry. Black dots represent Lagrangian particles. Particle sizes are sampled from the distribution in Figure 3. Particles shown in the figure are sampled from a 1 degree slice of space. The majority of the particles are concentrated in the near vent recirculating area. A smaller subset of particles is concentrated at the base of the propagating pyroclastic density current.

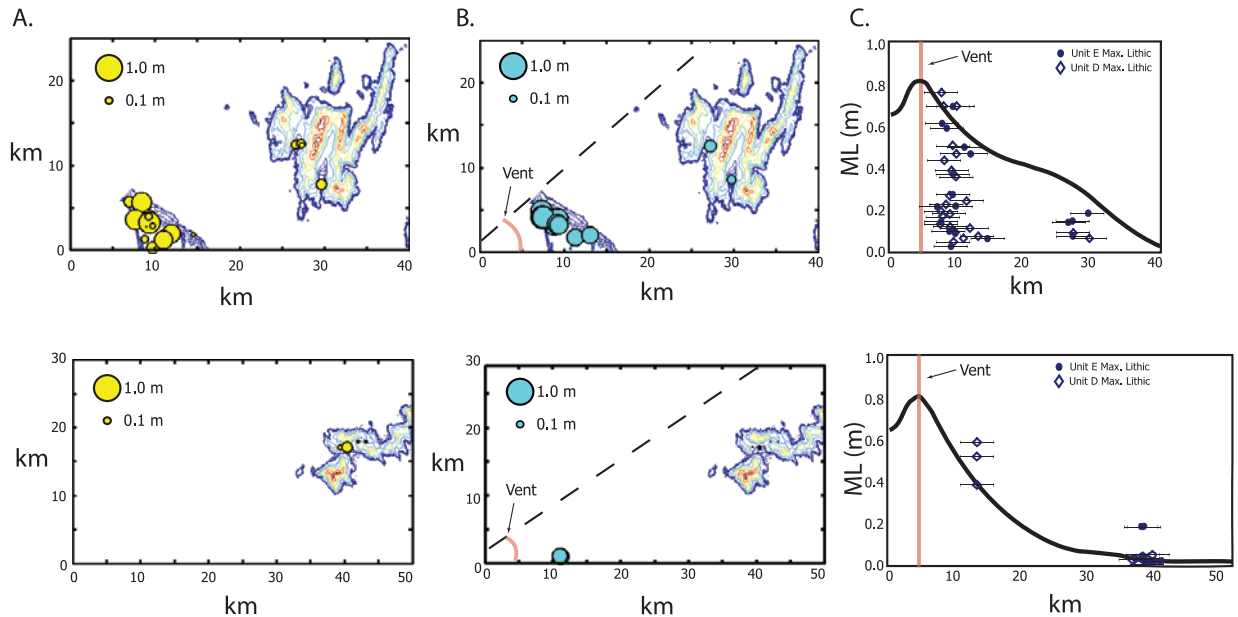


**Figure 12.** Maximum lithic distribution. Figure 12a (yellow symbols) shows the maximum lithic size measured from the KPT deposit, Unit E [Allen, 2001]. The size of the circular symbols corresponds to the maximum lithic size found at a location. The top map shows the area near Kos and north toward Kalymnos, while the bottom map shows Tilos. Figure 12b shows the synthetic maximum lithic sizes based on the Eulerian-Eulerian-Lagrangian (EEL) simulations with an eruptive flux of  $1.89 \times 10^6 \text{ m}^3/\text{s}$ . Again, the top map shows the north directed flows toward Kalymnos, and the bottom map shows the Tilos-directed flows. Figure 12c shows the mean maximum lithic size versus distance from the vent (solid black line) compared to maximum lithic sizes from unit D (diamonds) and unit E (solid squares). The top figure shows maximum lithic size for the Kalymnos trajectory, and the bottom figure shows the Tilos maximum lithic trends. These symbols are shown with a 5 km error bar to denote uncertainty in the vent location where they originated.

shorter. Certainly, if there were pauses between portions of the eruption, this would increase this timescale. But the volume and deposit distribution limitations require only around a day or less during the peak activity of this moderate to large volume eruption. The climate implications for such a short duration burst of particle-laden eruptive activity may be dramatic [Timmreck and Graf, 2006] and warrants further consideration.

[34] The lithic size distribution coupled with the distribution of finer material suggest that at the initiation of the large ignimbrite producing part of the eruption, the area north of Kos can be explained by saltation over a solid surface, while much of the area to the south was leaky and had a more rapid decay of maximum lithics from the vent. However, by the end of the ignimbrite producing phase (Unit E) the basal boundaries to the south are most consistent with saltation. This transition from leaky to saltation boundary condition suggests that there was some water present in the depression south of Kos, between the present-

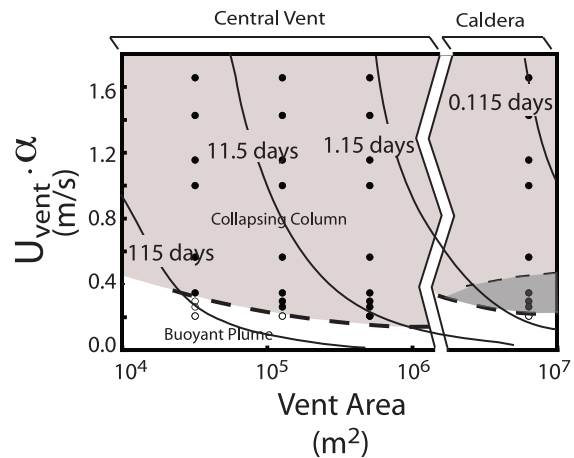


**Figure 13.** Regime diagram for eruptive conditions with lines of constant duration of eruption. The estimated eruption duration times were calculated using the volume of the deposits,  $60 \text{ km}^3$ . Simulated flows that had the range of KPT deposits (dark shaded region) imply minimum eruption duration of 0.35 to  $\sim 1.4$  days.

day island of Nisyros and Tilos, at the start of the eruption. Yet, this sea was either shallow and overcome by the preceding eruptive units, or a thick pumice raft developed during the course of the eruption that permitted much greater saltation efficiency toward the end of the eruption. While this coupled deposit-simulation approach cannot discern the depth of the water before the eruption, it does place the constraint that some water was likely present at the initiation of the eruption and this may help refine estimates of neotectonic subsidence in the area.

## Acknowledgments

[35] We thank Greg Valentine, Marie Edmonds, and Associate Editor Vincent Salters for their helpful reviews. We thank Sharon Allen for kindly sharing her data and introducing us to many of the outcrops of the KPT. Olivier Bachmann is thanked for his help in the field and many discussions of this work. This work was supported by a NASA Earth Systems Science Fellowship and Miller Institute Fellowship (J. D.) and NSF grant, EAR-0440391 (G. B.).

## References

- Agrawal, K., et al. (2001), The role of meso-scale structures in rapid gas-solid flows, *J. Fluid Mech.*, *445*, 151–185.
- Allen, S. R. (2001), Reconstruction of a major caldera-forming eruption from pyroclastic deposit characteristics: Kos Plateau Tuff, eastern Aegean Sea, *J. Volcanol. Geotherm. Res.*, *105*, 141–162.
- Allen, S. R., and R. A. F. Cas (2001), Transport of pyroclastic flows across the sea during explosive, rhyolitic eruption of the Kos Plateau Tuff, Greece, *Bull. Volcanol.*, *62*, 441–456.
- Allen, S. R., et al. (1999), Stratigraphy of the Kos Plateau Tuff: Product of a major Quaternary explosive rhyolitic eruption in the eastern Aegean, Greece, *Int. J. Earth Sci.*, *88*, 132–156.
- Benyahia, S., et al. (2005), Evaluation of boundary conditions used to model dilute, turbulent gas/solids flows in a pipe, *Powder Technol.*, *156*, 62–72.
- Branney, M. J., and P. Kokelaar (1997), Giant bed from a sustained catastrophic density current flowing over topography: Acatlan ignimbrite, Mexico, *Geology*, *25*, 115–118.
- Branney, M. J., and P. Kokelaar (2002), *Pyroclastic Density Currents and the Sedimentation of Ignimbrites*, *Geol. Soc. Mem.*, vol. 27, Geol. Soc., London.
- Burgisser, A. (2004), Physical volcanology of the 2050 BP caldera-forming eruption of Okmok Volcano, Alaska, *Bull. Volcanol.*, *67*, 497–525.
- Cagnoli, B., and M. Manga (2004), Granular mass flows and Coulomb's friction in shear cell experiments: Implications for geophysical flows, *J. Geophys. Res.*, *109*, F04005, doi:10.1029/2004JF000177.
- Carey, S., et al. (1996), Pyroclastic flows and surges over water: An example from the 1883 Krakatau eruption, *Bull. Volcanol.*, *57*, 493–511.
- Clarke, A. B., et al. (2002), Transient dynamics of vulcanian explosions and column collapse, *Nature*, *415*, 897–901.
- Darteville, S., W. I. Rose, J. Stix, K. Kelfoun, and J. W. Vallance (2004), Numerical modeling of geophysical granular flows: 2. Computer simulations of plinian clouds and pyroclastic flows and surges, *Geochem. Geophys. Geosyst.*, *5*, Q08004, doi:10.1029/2003GC000637.
- Dobran, F. (2001), *Volcanic Processes, Mechanisms in Material Transport*, 590 pp., Kluwer Acad., Norwell, Mass.
- Dobran, F., et al. (1994), Assessing the pyroclastic flow hazard at Vesuvius, *Nature*, *367*, 551–554.
- Druitt, T. H., and V. Francavigilia (1992), Caldera formation on Santorini and physiography of the islands in the late Bronze Age, *Bull. Volcanol.*, *54*, 484–493.
- Dufek, J., and G. W. Bergantz (2007), The suspended-load and bed-load transport of particle laden gravity currents: Insight from pyroclastic flows that traverse water, *J. Theor. Comput. Fluid Dyn.*, *21*, 119–145.
- Dufek, J. D., and G. W. Bergantz (2005), Transient two-dimensional dynamics in the upper conduit of a rhyolitic eruption: A comparison of the closure models for the granular stress, *J. Volcanol. Geotherm. Res.*, *143*, 113–132.
- Dufek, J., et al. (2007), Littoral blasts: Pumice-water heat transfer and the conditions for steam explosions when pyroclastic flows enter the ocean, *J. Geophys. Res.*, *112*, B11201, doi:10.1029/2006JB004910.
- Edmonds, M., and R. A. Herd (2005), Inland-directed base surge generated by the interaction of pyroclastic flows and seawater at Soufriere Hills volcano, Montserrat, *Geology*, *33*, 245–248.
- Fan, J., et al. (2000), Prediction of dense turbulent particle laden riser flow with a Eulerian and Lagrangian combined model, *Chem. Eng. Commun.*, *179*, 201–218.
- Fisher, R. V., et al. (1993), Mobility of a large-volume pyroclastic flow: Emplacement of the Campanian ignimbrite, Italy, *J. Volcanol. Geotherm. Res.*, *56*, 262–275.
- Freundt, A. (2003), Entrance of hot pyroclastic flows into the sea: Experimental observation, *Bull. Volcanol.*, *65*, 144–164.
- Gera, D., et al. (2004), Hydrodynamics of particle segregation in fluidized beds, *Int. J. Multiphase Flow*, *30*, 419–428.
- Giordano, G., and F. Dobran (1994), Computer simulations of the Tuscolano-Artemisios 2nd Pyroclastic Flow Unit (Alban Hills, Latium, Italy), *J. Volcanol. Geotherm. Res.*, *61*, 69–94.
- Johnson, P. C., and R. Jackson (1987), Frictional-collisional constitutive relations for granular materials, with application to plane shearing, *J. Fluid Mech.*, *176*, 67–93.
- LaCroix, A. (1904), *La Mintagne Pelee et Ses Eruptions*, Masson, Paris.
- Lun, C. K. K., et al. (1984), Kinetic theories for granular flow: Inelastic particles in Couette flow and slightly inelastic particles in a general flow field, *J. Fluid Mech.*, *140*, 223–256.
- Mastin, L. G., and J. B. Witter (2000), The hazards of eruptions through lakes and seawater, *J. Volcanol. Geotherm. Res.*, *97*, 195–214.
- Mattioli, G. S., et al. (2007), Unique and remarkable dilatometer measurements of pyroclastic flow-generated tsunamis, *Geology*, *35*, 25–28.
- Miller, T. P., and R. L. Smith (1977), Spectacular mobility of ash flows around Aniakchak and Fisher calderas, Alaska, *Geology*, *5*, 173–176.
- Neri, A., et al. (2002), Mass partition during collapsing and transitional columns by using numerical simulations, *J. Volcanol. Geotherm. Res.*, *115*, 1–18.
- National Oceanic and Atmospheric Administration (1976), *US Standard Atmosphere*, Washington, D. C.
- Papale, P., and F. Dobran (1994), Magma flow along the volcanic conduit during the Plinian and pyroclastic flow phases of the May 18, 1980, Mt. St. Helens eruption, *J. Geophys. Res.*, *99*, 4355–4373.



- Pe-Piper, G., et al. (2005), Neotectonics and the Kos Plateau Tuff eruption of 161 ka, South Aegean arc, *J. Volcanol. Geotherm. Res.*, *139*, 315–338.
- Peirano, E., and B. Leckner (1998), Fundamentals of turbulent gas-solid flows applied to circulating fluidized bed combustion, *Prog. Energy Combust. Sci.*, *24*, 259–296.
- Robin, C., M. Monzier, and J. P. Eissen (1994), Formation of the mid-fifteenth century Kuwae caldera (Vanuatu) by an initial hydroclastic and subsequent ignimbrite eruption, *Bull. Volcanol.*, *56*, 170–183.
- Savage, S. B. (1998), Analyses of slow high-concentration flows of granular materials, *J. Fluid Mech.*, *377*, 1–26.
- Syamlal, M. (1987), A review of granular stress constitutive relations, pp. 21,353–22,372, U. S. Dept. of Energy, Springfield, Va.
- Syamlal, M., et al. (1993), MFIx Documentation: Theory Guide, technical note, 49 pp., U. S. Dept. of Energy, Morgantown, W. Va.
- Timmreck, C., and H. F. Graf (2006), The initial dispersal and radiative forcing of a Northern Hemisphere mid-latitude super volcano: A model study, *Atmos. Chem. Phys.*, *6*, 35–49.
- Todesco, M., A. Neri, T. Esposti Ongaro, P. Papale, and M. Rosi (2006), Pyroclastic flow dynamics and hazard in a caldera setting: Application to Phlegrean Fields (Italy), *Geochem. Geophys. Geosyst.*, *7*, Q11003, doi:10.1029/2006GC001314.
- Valentine, G. A. (1987), Stratified flow in pyroclastic surges, *Bull. Volcanol.*, *49*, 616–630.
- Valentine, G. A., and K. H. Wohletz (1989), Numerical models of Plinian eruption columns and pyroclastic flows, *J. Geophys. Res.*, *94*, 1867–1887.
- Watts, P., and C. F. Waythomas (2003), Theoretical analysis of tsunami generation by pyroclastic flows, *J. Geophys. Res.*, *108*(B12), 2563, doi:10.1029/2002JB002265.
- Whitham, A. G., and R. S. J. Sparks (1986), Pumice, *Bull. Volcanol.*, *48*, 209–223.
- Wilson, C. J. N., and W. Hildreth (2003), Assembling an ignimbrite: Mechanical and thermal building blocks in the Bishop Tuff, California, *J. Geol.*, *111*, 653–670.
- Zimanowski, B., et al. (1997), Premixing of magma and water in MFCI experiments, *Bull. Volcanol.*, *58*, 491–495.